Editors' Suggestion

In-vacuum thin eddy-current septum magnet for innovative off-axis beam injection in next-generation light source

Shiro Takano,[1,2,*] Kenji Fukami,[1,2] Takahiro Inagaki,[2,1] Taiki Iwashita,[3,4] Chikara Kondo,[1,2] Mitsuhiro Masaki,[1] Kanichiro Ogata,[5] Masaya Oishi,[1,2] Yoshiyuki Saito,[5] Masazumi Shoji,[1,2] Minori Tajima,[1] Kazuhiro Tamura,[1,2] Tsutomu Taniuchi,[1] Takahiro Watanabe,[1,2] Hiroshi Yamaguchi,[1] and Hitoshi Tanaka[2]

[1]*Japan Synchrotron Radiation Research Institute (JASRI), 1-1-1 Kouto, Sayo, Hyogo 679-5198, Japan*
[2]*RIKEN SPring-8 Center (RSC), 1-1-1 Kouto, Sayo, Hyogo 679-5148, Japan*
[3]*NAT Corporation, 5-146 Shirono, Muramatsu, Tokai, Ibaraki 319-1112, Japan*
[4]*National Institutes for Quantum Science and Technology (QST), 6-6-11-901 Aramaki Aoba, Aoba, Sendai, Miyagi 980-8579, Japan*
[5]*TOKIN Corporation, 7-1-1 Asahicho, Shiroishi, Miyagi 989-0223, Japan*

(Received 6 March 2025; accepted 18 August 2025; published 10 September 2025)

Beam injection is one of the most crucial issues for next-generation light sources such as diffraction-limited storage rings. We propose a novel transparent off-axis beam injection scheme for low-emittance storage rings of future light sources. The scheme aims to achieve efficient beam injection into a narrow dynamic aperture with small injection amplitude, while minimizing perturbation to the stored beam with transparent beam injection. An in-vacuum thin eddy-current septum magnet is one of the key components of the scheme to achieve the small injection amplitude. A prototype of the magnet with an accommodating ultrahigh vacuum (UHV) chamber was designed and fabricated. Magnet performance of the prototype demonstrated that an injection amplitude as small as 3 mm is feasible, fulfilling the tight constraint of injection amplitude in off-axis beam injection for next-generation light sources. The prototype achieved a UHV pressure of better than 1×10^{-7} Pa, ensuring the vacuum performance required for stable operation in storage rings.

DOI: 10.1103/rvbw-ml5n

I. INTRODUCTION

Light sources have been striving to enhance their performance, pursuing higher photon brilliance and coherence [1–4]. This trend has been pushing the lattice design of a storage ring toward a diffraction-limited beam emittance, which naturally results in a smaller dynamic aperture of the ring than ever before [5] and a narrower acceptance for the injected beam.

Beam injection for a light source ring is required to accumulate a designated beam current and maintain a constant beam current by implementing top-up or other measures. Challenges of beam injection for next-generation diffraction-limited light sources are (i) efficient beam injection into the narrow dynamic aperture of the storage ring by minimizing the injection amplitude, i.e., the oscillation amplitude of the injected beam in the storage ring, (ii) transparent beam injection to the photon users with minimized transient stored beam oscillation upon the beam injection, and (iii) top-up or alternate means to maintain the required beam intensity. Various advanced beam injection schemes have been successfully implemented. These include nonlinear kickers [6–9] for transparent off-axis injection, on-axis swap-out injection [10,11] for rings with limited dynamic apertures, and on-axis off-energy injection [12,13]. These techniques provide solutions tailored to the specific constraints of a given light source such as its dynamic aperture and injector characteristics.

We propose a novel off-axis beam injection scheme [14] for SPring-8-II [3], the ongoing high-brilliance and high-coherence upgrade of SPring-8. The limited dynamic aperture and suppressed linear dispersion of the new ring precluded the use of the nonlinear kicker or off-energy injection methods. Our scheme is specifically designed to leverage the SACLA linear accelerator as a high-performance, low-emittance injector. Building upon the upgrades to the current SPring-8 off-axis injection system, which enabled its present stable and reliable top-up operation [15], our proposed scheme will minimize the injection amplitude and ensure a transparent top-up capability.

*Contact author: takano@spring8.or.jp

Published by the American Physical Society under the terms of the Creative Commons Attribution 4.0 International license. Further distribution of this work must maintain attribution to the author(s) and the published article's title, journal citation, and DOI.

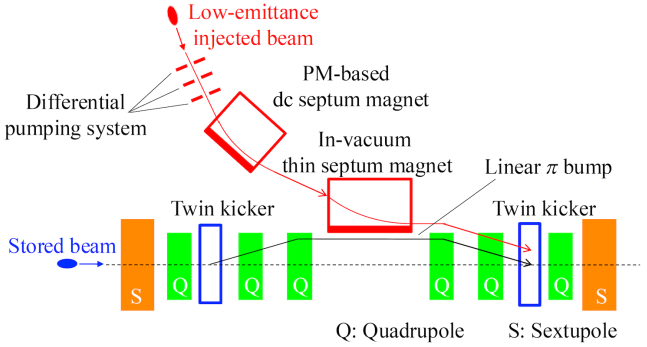


FIG. 1. Schematic layout of the proposed transparent off-axis beam injection for next-generation light sources.

A schematic setup for the proposed beam injection scheme is illustrated in Fig. 1. It features an in-vacuum septum magnet and direct injection without a vacuum window. To cope with the small acceptance in beam injection, a low emittance of the injected beam is necessary. A full-energy on-demand beam injection from the SACLA linear accelerator to the current SPring-8 storage ring has been developed [16] and is already in operation. We will capitalize on the low-emittance beam from the high-performance SACLA linear accelerator, which will serve as a full-time low-emittance beam injector of SPring-8-II while delivering x-ray free-electron laser photon beams to users. The beam delivered from the SACLA linear accelerator will go through a differential pumping system, which connects the low pressure of the beam transport line and the ultrahigh vacuum (UHV) comparable to that of the storage ring without a vacuum window that could deteriorate the small beam emittance. Septum magnets will deflect the injected beam toward the off-axis beam injection point of the storage ring. Two identical kicker magnets of the same kick angle, twin kicker magnets, will be placed in the beam injection section of the storage ring to provide an orbit bump for off-axis beam injection. A so-called π-bump scheme will be adopted, wherein the twin kickers are deployed π rad apart in the betatron phase to create a closed orbit bump. Nonlinear magnets, such as sextupoles, will be excluded from the orbit bump. This feature ensures the bump closure at any time during beam injection, which is essential to securing transparent beam injection to photon users.

Three key components to be employed in the proposed off-axis beam injection scheme are (1) the permanent magnet (PM) based dc septum magnet for energy saving, (2) the in-vacuum thin septum magnet for achieving the small injection amplitude, and (3) the twin kicker magnets for the transparent beam injection. Prototypes of the PM-based dc septum magnet [17], the twin kicker magnets [18], and a precision solid-state pulser [19] for the kickers have been developed and successfully demonstrated. The kicker magnets are used with ceramic vacuum chambers with an inner metallic coating. Eddy current induced in the coating during magnet excitation is an issue that can affect the magnetic field of the kicker. A prototype of the ceramic vacuum chamber with an eddy current-suppressed metallic coating has been developed and is undergoing performance verification, which will be reported elsewhere.

This paper reports on the demonstration of a prototype in-vacuum thin eddy-current septum magnet developed for the new off-axis beam injection we propose. Section II elaborates on the concepts and details of magnet and vacuum design. Magnet and vacuum performance are presented in Secs. III and IV, respectively.

II. DESIGN

The minimum possible injection amplitude in the off-axis beam injection is dictated by the emittance of both injected and stored beams and by the mechanical design of the septum magnet that is located at the end of the beam injection line. In the new off-axis beam injection that we propose for the low-emittance storage ring of SPring-8-II, we are going to capitalize on the low-emittance beam from the high-performance SACLA linac [16] and employ an in-vacuum thin eddy-current septum magnet. An in-vacuum eddy-current septum magnet [20–22] helps reduce the injection amplitude by eliminating the walls of the vacuum chamber between injected and stored beams that exist in the case of an out-of-vacuum septum magnet. Our goal is to achieve an injection amplitude of a few millimeters through a thin design of the eddy-current septum.

Schematics of the in-vacuum thin eddy-current septum magnet developed in this work are illustrated in Fig. 2. It consists of a pulsed septum magnet, an rf shield, a magnetic shield, and a UHV chamber. The pulsed septum magnet,

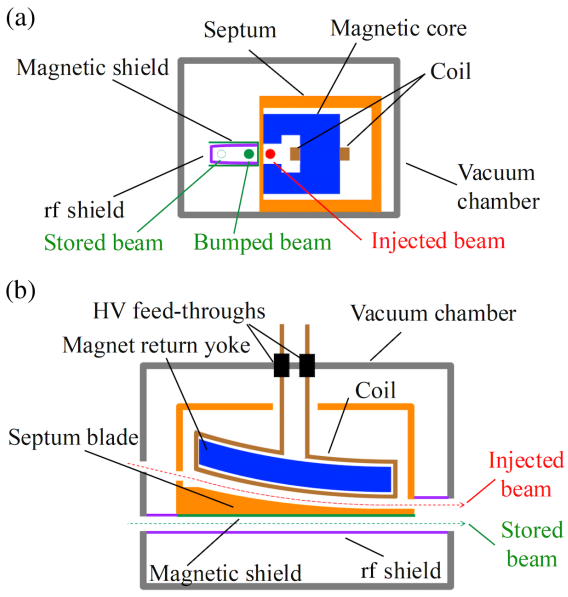


FIG. 2. Schematics of an in-vacuum thin eddy-current septum magnet. (a) Cross section perpendicular to the beam trajectories. (b) Cross section in the plane of the beam trajectories.

TABLE I. Target specifications for the in-vacuum thin eddy-current septum magnet.

Parameter	Value
Magnetic field	1.4 T
Magnetic pole length	500 mm
Septum thickness[a]	0.5 mm
Magnetic shield thickness	0.5 mm or less
Stray field	$< 10^{-5}$ T m
Pressure	$< 10^{-7}$ Pa

[a]At the beam injection point into a storage ring.

which deflects the injected beam, has a box-shaped septum enclosing the whole magnet. Eddy current induced in the septum during magnet excitation helps reduce the leakage of the magnetic field to the stored beam. The part of the septum in the median plane that separates the injected beam from the stored beam is referred to as a septum blade in this article. The rf shield is an enclosure that allows the stored beam to pass through while containing the electromagnetic field accompanying the stored beam. A magnetic shield is placed outside the rf shield to reduce the stray field to the stored beam to a tolerable level for transparent beam injection. Thin designs of the septum blade and the magnetic shield on the rf shield are required to ensure the small injection amplitude. A UHV chamber houses the pulsed septum magnet and the rf shield. Target specifications of the in-vacuum thin eddy-current septum magnet of this work are summarized in Table I. Magnet and vacuum design details are presented below, focusing on those relevant to beam injection performance.

A. Magnet design

The pulsed septum magnet of this work consists of a magnetic core, an excitation coil, and the septum (Fig. 2). The design parameters of the magnet are summarized in Table II. A distinct feature of the eddy-current septum magnet of this work is the thin design of the septum blade, as thin as 0.5 mm at the beam injection point, to ensure the small injection amplitude. The excitation pulse length is a compromise between the shielding effect of the eddy current induced in the septum and the high voltage applied to the excitation coil. A half-sine wave of 10 μs was chosen as the excitation pulse shape. The corresponding skin depth is 0.3 mm, which is less than the minimum thickness of the septum blade.

TABLE II. Design parameters of the pulsed septum magnet.

Parameter	Value
Magnetic field	1.4 T
Magnetic pole length	500 mm
Pole gap	2 mm
Core material	Electrical steel sheet (0.1 mm thick)
Coil turn number	1
Peak current	2.3 kA
Pulse width	10 μs (half-sine wave excitation)
Septum thickness	0.5[a]–18[b] mm
Magnetic shield thickness	0.5 mm or less
Stray field	$< 10^{-5}$ T m
Repetition rate	10 Hz

[a]At the exit of the magnetic core, i.e., the beam injection point into a storage ring.
[b]At the entry of the magnetic core.

A laminated magnetic core of 0.1 mm thick electric steel sheets was designed to ensure a pulsed magnetic field of 1.4 T in the magnetic pole gap. A nonoriented silicon steel sheet coated with a glass-based insulator (Nikkindenji Kogyo, ST-100) was selected as it has a saturation flux density as high as 1.6 T. The geometry of the magnetic pole was optimized to achieve a flat magnetic field distribution as close to the septum blade as possible. The magnetic core has a C-type configuration with a pole gap of 2 mm. The shape of the silicon steel sheet that determines the cross-sectional shape of the laminated magnetic core is illustrated in Fig. 3. In order to obtain a flat field distribution toward the septum blade, the allowable maximum chamfer of the septum-side magnetic pole corner was set to C0.2. The gap dimension tolerance was set to preclude a larger gap on the septum side.

The longitudinal geometry of the magnetic core was designed with a curved shape that follows the curved electron beam trajectory in the magnetic pole gap (Fig. 2). The major advantage of the curved core shape is that it allows for a thicker septum blade toward the injected beam entry side, resulting in an effective reduction of magnetic field leakage. The steel sheets are stacked in the core by shifting them transversely to follow the curved beam trajectory. In the prototype development of this work, the curvature of the core was adapted to an electron energy of 3 GeV, instead of the 6 GeV for SPring-8-II, to confirm that the curved core can be properly assembled even when

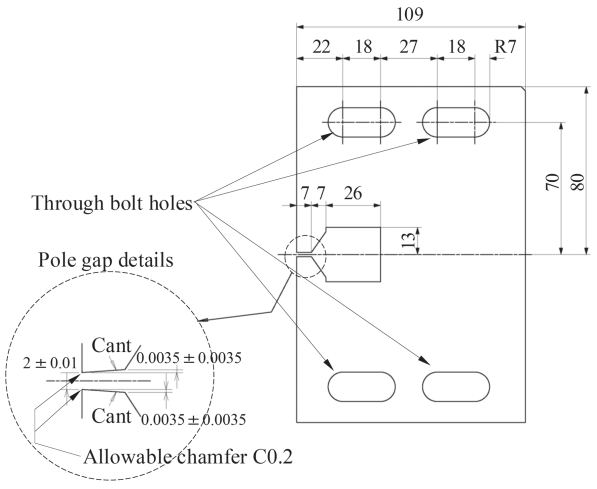


FIG. 3. Cross-sectional shape of the magnetic core.

the bend of beam trajectory in the core becomes larger, as in the case of lower energy light sources. Fabrication of the magnet for use in SPring-8-II will be more straightforward than the present prototype. Suppressing outgassing from the magnetic core is crucial to achieving a UHV pressure better than 10^{-7} Pa, which is necessary for use in a storage ring. Any small gaps in the laminated core must be eliminated to prevent air from being trapped and leaking into the vacuum after evacuation. Two plates made of 316L stainless steel are placed on the longitudinal ends of the laminated magnetic core to hold the core between them. Four bolts penetrate the magnetic core (Fig. 3) to secure the end plates, allowing the steel plates inside the core to be firmly fixed without the use of adhesives. The bolts are made of 316L stainless steel and covered with polyimide films to provide electrical insulation from the magnetic core.

A one-turn excitation coil made of oxygen-free copper is mounted on the magnetic return yoke, as schematically illustrated in Fig. 2. The coil is encased in ceramic insulator blocks that isolate the coil and the magnetic core up to 20 kV. The ceramic coil insulators are fixed to the stainless steel end plates outside the magnetic core to support the coil.

The septum is made of oxygen-free copper, making it suitable for use in a UHV. Its shape was designed to enclose the entire magnetic core, as schematically illustrated in Fig. 2, to minimize the leakage of stray magnetic field into the stored beam region. The thickness of the septum blade is 0.5 and 18 mm at the beam exit and entry ends of the magnetic core, respectively, corresponding to the curved magnetic core shape. The septum blade and core are separated by a 50 μm thick polyimide film, which prevents electrical conduction between the layers in the laminated core through the septum blade. The appearance of the septum containing the pulsed magnet is shown in Fig. 4.

B. Vacuum design

The external appearance of the vacuum chamber is illustrated in Fig. 5. The vacuum chamber houses the pulsed septum magnet that deflects the injected beam and the rf shield that allows the stored beam to pass through with low impedance. The layout of the inside of the vacuum chamber is shown in Fig. 6. The magnet is fixed to the bottom of the vacuum chamber. The top of the vacuum chamber can be removed like a lid, facilitating the installation of the magnet, the rf shield, and other items inside the vacuum chamber. The vacuum chamber, including the top face lid, is made of stainless steel. The lid is sealed with a metal O-ring.

The rf shield is made of oxygen-free copper. The shape of the rf shield was designed taking into account the effect of coupling impedance and heating due to the wall current induced by the stored beam. Figure 7 shows the structure of the rf shield. The rf shield is fixed to the septum by brackets

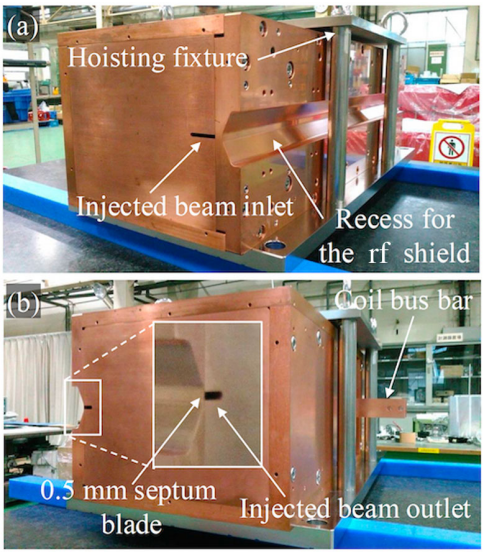


FIG. 4. Box-shaped septum containing the pulsed magnet, viewed from the injected beam entry side (a) and the injected beam exit side (b). The hoisting fixture is to be removed after installation in the vacuum chamber.

as shown in Fig. 7(b). To attenuate the magnetic field leakage to the stored beam orbit, a magnetic shielding sheet of material such as permalloy up to 0.5 mm thick is applied to the outer surface of the rf shield (Fig. 8).

Cooling was considered to deal with the heat generated by the stored beam-driven wall current on the rf shield, the

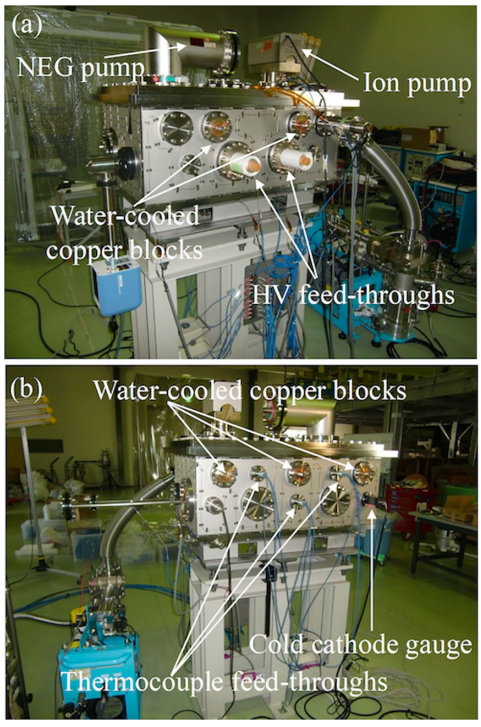


FIG. 5. External appearance of the vacuum chamber viewed from the HV feed-through side (a) and the opposite side (b).

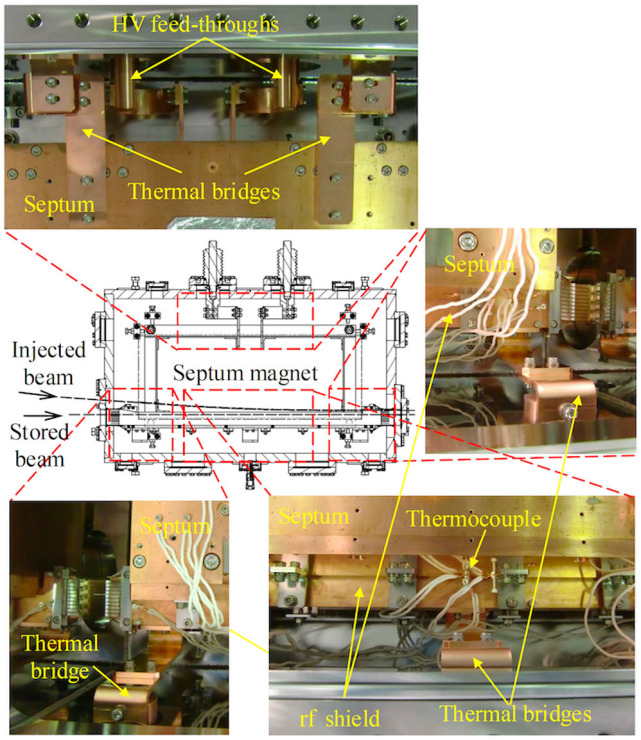


FIG. 6. Layout of the inside of the vacuum chamber.

excitation current of the coil, and the eddy current induced in the septum during magnet excitation. An indirect cooling structure employing water cooling outside the vacuum was designed for the rf shield and the septum wall. Water-cooled copper blocks are mounted on the side of the vacuum chamber (Fig. 5). These blocks are connected to the rf shield and the septum wall with oxygen-free copper thermal bridges (Fig. 6) to remove the heat. The excitation coil of the pulsed septum is connected to two high-voltage feed-throughs (KYOCERA, C330K808ACU1) mounted on the side of the vacuum chamber (Fig. 5). The flanges of the feed-throughs are water-cooled to cool the coil indirectly. Type K thermocouples are attached to the rf shield and the septum for temperature measurement (Fig. 6).

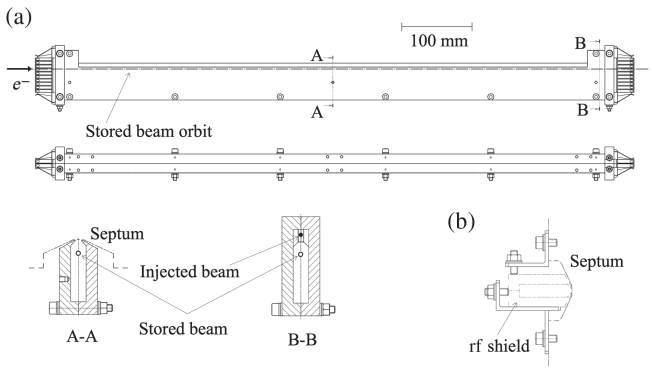


FIG. 7. Rf shield (a) and brackets for fixing it to the magnet (b).

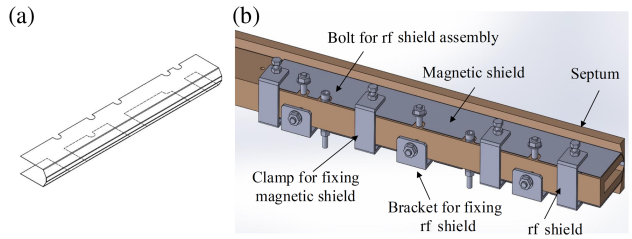


FIG. 8. Example of magnetic shielding sheet (a) and its attachment to the rf shield (b).

A combination of a nonevaporating getter (NEG) pump (SAES Getters, CapaciTorr D2000) and a small ion pump with a pumping speed of 60 L/s is integrated into the lid of the vacuum chamber to evacuate the inside (Fig. 5). The NEG pump is placed in an L-shaped container attached to the lid so that the radiation emitted from the NEG, which reaches temperatures of up to 450 °C during activation, does not directly impact the magnet. The vacuum chamber is equipped with a cold cathode gauge (MIRAPRO, Cold Cathode Tough Gauge) that is capable of measuring pressures down to 1×10^{-8} Pa.

III. MAGNET PERFORMANCE

The magnet performance of the pulsed septum magnet was examined in the atmosphere prior to its installation in the vacuum chamber. The prototype solid-state pulsed power supply developed in a separate work [19] was employed after the capacitors of the main charger were adjusted to the magnet of this work. The pulsed septum magnet was successfully excited with the designed peak current of 2.3 kA and the pulse width of 10 μs without any failures, such as electrical discharges.

A. Deflection magnetic field

One of the keys to achieving small injection amplitude is a transversely uniform magnetic field in the magnetic pole to deflect the injected beam near the septum blade. Calculated lateral magnetic field distributions in the pole gap are shown in Fig. 9. To take the effect of the eddy current induced in the septum into account, time-domain simulations were performed with two-dimensional models corresponding to each end of the magnetic core. A three-dimensional electromagnetic field analysis software, CST Studio Suite [23], was utilized for all the simulations performed in this paper. Figures 9(a) and 9(b) show the models for the injected beam entry side with a septum blade thickness of 18 mm and the exit side with a thickness of 0.5 mm, respectively. The magnetic core was modeled using iron with resistivity intentionally set to infinity to simulate a laminated structure. In the calculations of Fig. 9(c), the septum-side magnetic pole corners were assumed to have sharp edges without chamfers. The lateral magnetic field distributions against the distance from the septum

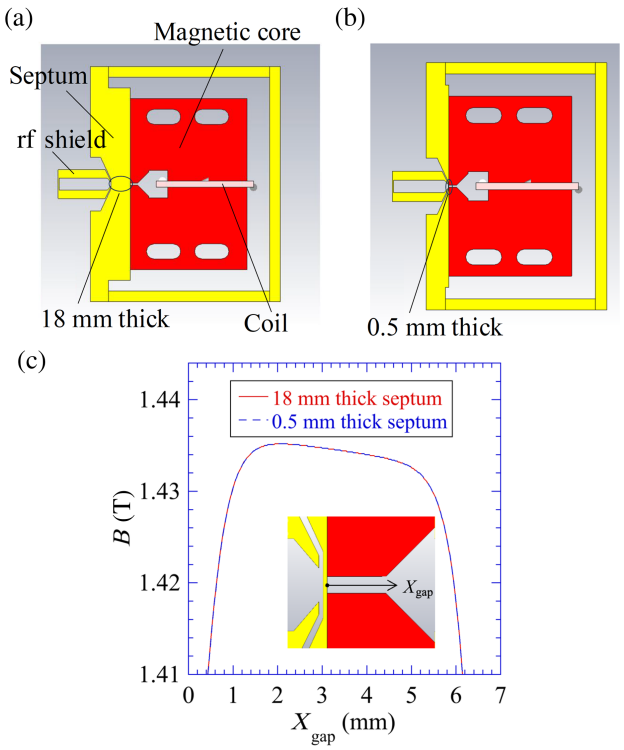
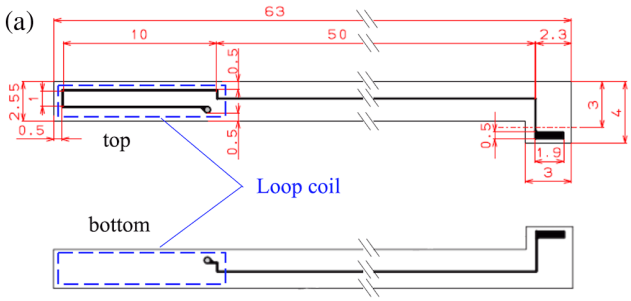


FIG. 9. Lateral magnetic field distribution in the magnetic pole gap. Two-dimensional simulation models for the injected beam entry end with 18 mm thick septum (a) and the exit end with 0.5 mm thick septum (b). Simulation results (c).



(b)

Layer stack-up		thickness (μm)
Top	Solder mask	20
	Copper	32
	Core	60
Bottom	Copper	32
	Solder mask	20

FIG. 10. Thin search coil for gap magnetic field measurement on the upstream side of the pulsed magnet. (a) Circuit board patterns and (b) layer stack-up. A similar one with a mirror-symmetrical shape was used on the downstream side.

blade calculated at the excitation peak of the magnet are illustrated in Fig. 9(c). The field distribution was found to be independent of the septum blade thickness between 0.5 and 18 mm, maintaining the deflecting magnetic field even when the injected beam is brought as close as 1 mm to the septum blade.

Measuring the magnetic field in the pole gap of 2 mm presented a significant technical challenge. Thin search coils were designed and fabricated to measure the magnetic field in the narrow gap. A schematic of the search coil is illustrated in Fig. 10. A single-turn rectangular loop coil, 10 mm long and 1 mm wide, was integrated into a thin, flexible printed circuit board with a total thickness of 164 μm. Two mirror-symmetric search coils were prepared, one for the upstream side of the pulsed septum magnet and the other for the downstream side. The setup for the gap field measurement is shown in Fig. 11. Each search coil was mounted on a 300 mm long, 1 mm thick ceramic guide, which was then placed in the pole gap with the long side of the rectangular coil aligned with the longitudinal direction of the magnetic core. The ceramic guide was moved by linear stages located outside the septum to measure the field distribution in the pole gap. The position of the ceramic guide in the pole gap was checked with a 1 mm diameter borescope inserted from the opposite end of the magnet. The excitation current of the magnet was simultaneously measured by a current transformer (CT) (Pearson Electronics, Model 1025).

The transverse magnetic field distribution in the pole gap was measured near both the injected beam entry and exit ends of the magnetic core. The distance of the longitudinal search coil center from the end of the magnetic core was 11.3 and 47.1 mm for the beam entry and exit sides, respectively. The excitation current measured by the CT

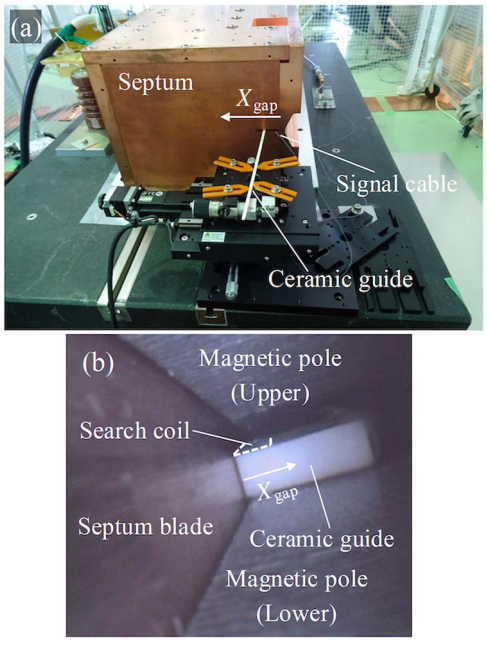


FIG. 11. Setup for magnetic field measurement in the magnetic pole gap. (a) The entire setup for the beam entry side and (b) inside the pole gap on the beam exit side as observed with the borescope inserted from the beam entry side.

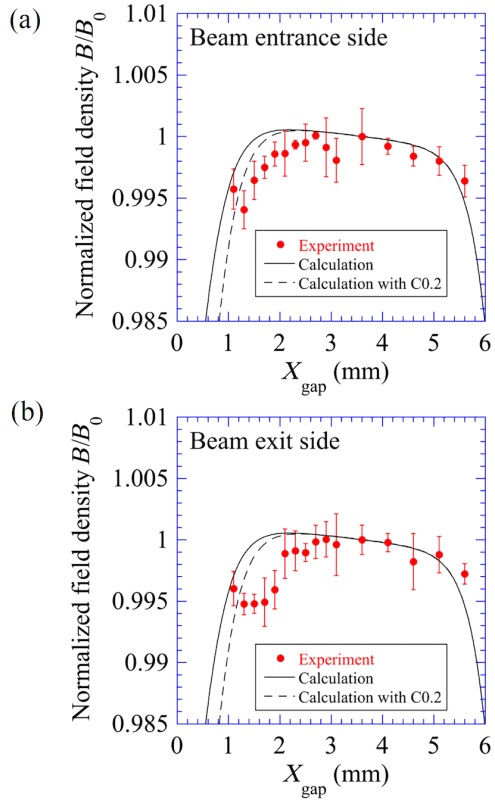


FIG. 12. Lateral distribution of the magnetic field in the pole gap measured near the beam entrance (a) and exit (b) of the magnetic core, along with the calculations.

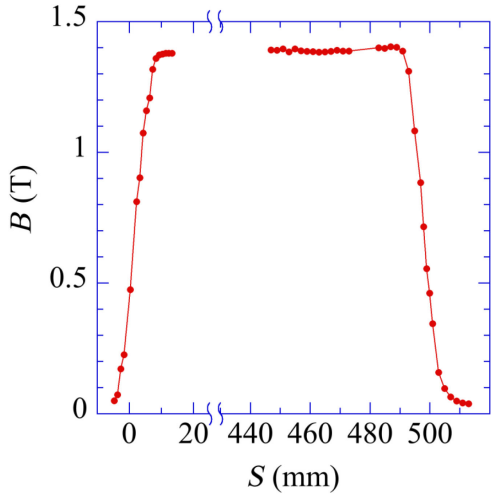


FIG. 13. Longitudinal distribution of the magnetic field in the magnetic pole gap.

was 2.28 kA. The measured lateral magnetic field distributions are shown in Figs. 12(a) and 12(b) as a function of the distance of the coil center from the septum blade X_{gap}. The positioning precision of the ceramic guide is better than 0.1 mm, which is sufficient to characterize the lateral distribution of the magnetic field in the pole gap shown in Figs. 12(a) and 12(b). The flux density at the peak timing of magnet excitation was obtained by averaging over the search coil area and then normalized by the value measured at a position of $X_{gap} = 3.6$ mm, near the center of the 7 mm wide magnetic pole. It was experimentally confirmed that the magnetic field strength at the center of the pole width remains within a 0.5% decrease even when the distance to the septum blade approaches 1 mm.

Calculated field distributions are also presented as solid lines in Figs. 12(a) and 12(b), which were derived from the simulations shown in Fig. 9(c) after averaging over the search coil width. The measured lateral flatness of the magnetic field in the gap was found to be consistent with the design-based simulations. The experimental data presented in Figs. 12(a) and 12(b) exhibited slight deviations from the calculated values, which did not have a significant impact on the performance of the magnet. These deviations appeared to be marginally larger than the statistical error bars in the range of 1 to 2 mm from the septum blade. The deviations can be partly attributed to chamfers on the septum-side magnetic pole corners (Fig. 3). For reference, the magnetic field distributions calculated with the maximum allowable chamfer of C0.2 are shown as dashed lines in Figs. 12(a) and 12(b).

The longitudinal distribution of the magnetic field in the pole gap was measured near the ends of the magnetic core using the setup of Fig. 11. The lateral position of the transverse search coil center was set at 1.1 mm from the septum blade. The longitudinal position of the search coil was moved along the curved surface of the septum blade while maintaining its distance from the blade. The measured longitudinal field distribution is shown in Fig. 13. The horizontal axis represents the location of the longitudinal center of the search coil. The injected beam entry and exit ends of the magnetic core correspond to $S = 0$ and 500 mm, respectively. To evaluate the integrated deflection magnetic field along the beam path in the pole gap, it is necessary to estimate the missing magnetic field values in the inner part of the magnetic core of Fig. 13 by interpolation. Linear interpolation of the missing data resulted in an experimental integrated magnetic field value of 0.69 T m, which is consistent with the design value of 0.7 T m. The small deviation is systematic rather than a random shot-to-shot fluctuation and is well within the correction capabilities of our system. The pulsed power supply can be fine-tuned to adjust the integrated field.

B. Stray magnetic field

Another key to achieving small injection amplitude is to reduce stray magnetic field leakage to the stored beam. According to simulations, the stray field in the region adjacent to the upstream half of the magnetic core, where the septum blade is relatively thick (see Fig. 2), was found to be as low as the geomagnetic level and negligible. Before the rf shield was attached, the stray magnetic field of the septum magnet was measured in the region adjacent to the

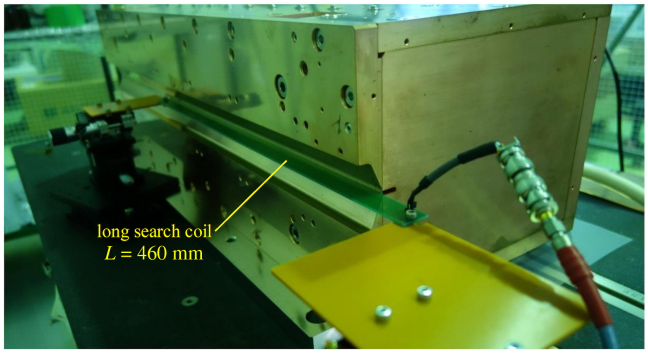


FIG. 14. Setup for stray magnetic field measurement.

downstream half of the magnetic core. The setup for leakage field measurement is shown in Fig. 14. Search coils of 460 mm length were placed in the median plane and aligned to be parallel to the outer straight surface of the septum blade. Of the 460, 300 mm covered the region adjacent to the downstream side of the magnetic core. The remaining 160 mm covered the area further downstream from the longitudinal edge of the magnetic core to detect stray field leakage downstream of the magnetic core. The leakage magnetic field was measured as the integrated value along the straight line parallel to the septum blade. Three types of 460 mm long search coils with widths of 0.5, 5, and 10 mm were employed according to the lateral distance from the septum blade. The shortest possible distance of the coil width center from the septum blade was 1.4, 3.65, and 6.15 mm for the 0.5, 5, and 10 mm wide search coils, respectively. To measure the stray field distribution as a function of distance from the septum blade, the 0.5 mm wide coil was moved 0.5, 1, 2, 3, 4, and 5 mm from the closest position to the septum blade. The 5 and 10 mm wide coils were moved 1, 2, 3, 4, 5, and 6 mm from their respective closest positions.

The measured stray magnetic field is shown in Fig. 15 as a function of time. The peak time of the 10 μs half sinusoidal excitation of the pulsed septum magnet corresponds to the time $t = 5$ μs. The integrated stray magnetic field averaged over the coil width is exhibited in Fig. 15 against the distance between the coil width center and the outer surface of the septum blade. The peak time of the stray magnetic field was significantly delayed from that of the magnetic excitation due to the effects of the eddy current induced in the septum. At a distance of 1.4 mm from the septum blade, the closest position for the measurement, the observed peak time of the integrated stray magnetic field was at $t = 22$ μs, which was in agreement with the 20 μs obtained by the simulation. The observed peak times appeared to increase with increasing distance from the septum blade, which was also consistent with the simulations.

First, we discuss the peak value of the integrated stray magnetic field. The experimentally obtained distribution of

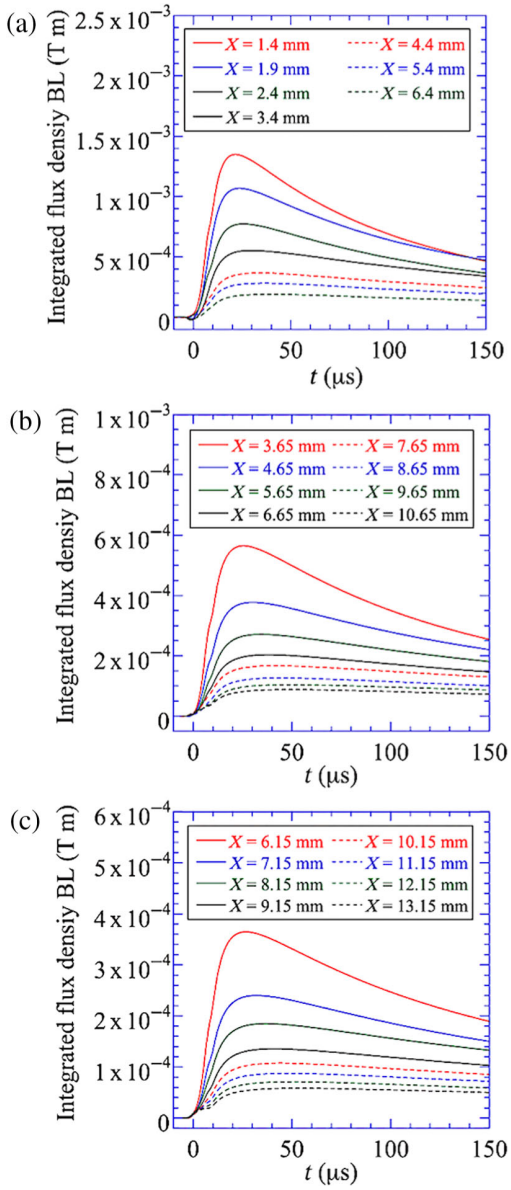


FIG. 15. Stray magnetic field as a function of time measured with long search coils of 0.5 mm (a), 5 mm (b), and 10 mm (c) wide, respectively, by changing the lateral distance from the septum blade. The integrated magnetic field was averaged over the coil width. The distance X from the septum blade is shown with respect to the center of the coil width.

the peak stray field against the distance from the septum blade is illustrated in Fig. 16. The stray field distributions derived from the three search coils were consistent with each other. In this semilogarithmic graph, which employs a linear scale for the distance from the septum blade, the measurements are approximately linearly aligned, thereby indicating a quasiexponential decay with respect to the distance. The results of simulations for the peak value of the stray magnetic field are also presented in Fig. 16. The experimental results were consistent with the simulation

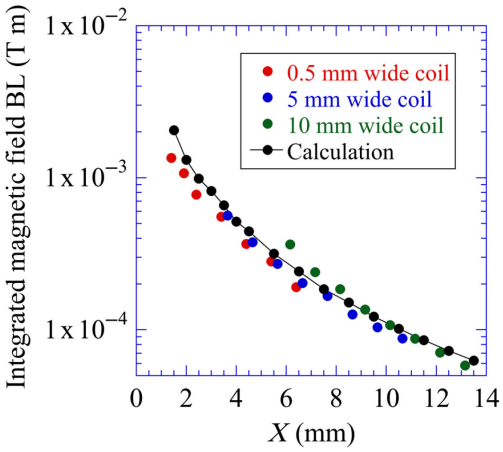


FIG. 16. Stray magnetic field measured as a function of the distance from the septum blade and the simulations. Peak values of data are presented as the integrated field averaged over the coil width. The distance X from the septum blade is shown with respect to the center of the coil width.

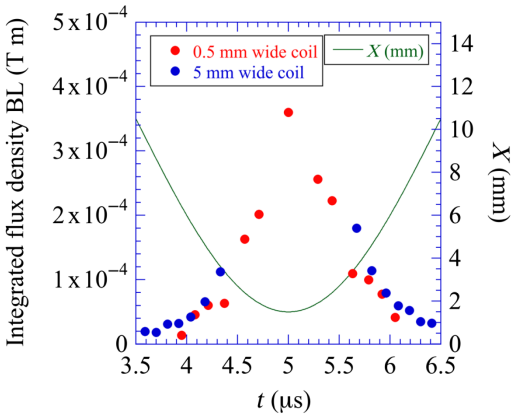


FIG. 17. Time-dependent stray magnetic field on the bumped orbit for beam injection derived from the data obtained with the 0.5 and 5 mm wide search coils in Figs. 15(a) and 15(b). The position X of the bumped stored beam is shown as the distance from the septum blade on the vertical axis to the right.

results, indicating that the septum box has been properly fabricated to suppress the stray field as designed.

In off-axis beam injection, pulsed orbit bumps are generated to bring the stored beam orbit closer to the injected beam. Therefore, the impact of the stray magnetic field on the beam injection performance should be evaluated considering the orbit bump during beam injection. We assumed the parameters listed in Table III for the stored beam orbit and the orbit bump to assess the stray magnetic field. Time-dependent stray magnetic field acting on the bumped stored beam was experimentally derived from the data obtained with the 0.5 and 5 mm wide search coils shown in Figs. 15(a) and 15(b). The results are shown in Fig. 17.

The value of the stray field at the position of $X = 1.5$ mm, corresponding to the orbit bump maximum, quotes the data of $X = 1.4$ mm in Fig. 15(a). The excitation peak of the pulsed septum magnet, when the orbit bump also reaches its maximum, corresponds to the time $t = 5$ μs. The stray field exerting the stored beam reaches a maximum of 3.6×10^{-4} T m at the time of the orbit bump maximum. The beam is located at a distance of 1.5 mm from the septum blade at this time. After the orbit bump, the stored beam returns to its original position at $X = 10.5$ mm. As shown in Figs. 15(b), 15(c), and 16, the stray magnetic field at this position peaks at about 1×10^{-4} T m around $t = 40$ μs. A magnetic shielding sheet up to 0.5 mm thick is supposed to be applied to the outer surface of the rf shield, as illustrated in Fig. 8. The magnetic shield needs to attenuate the stray field by a factor of 36 or more to meet our stray field goal of 1×10^{-5} T m.

To study the feasibility of magnetic shielding on the rf shield, we employed 0.3 mm thick sheets of permalloy (Ni80Fe20). The setup for the experiment is illustrated in Fig. 18. Each sheet is 30 mm by 100 mm, folded into

TABLE III. Orbit parameters for evaluation of magnet performance for beam injection.

Parameter	Value
Stored beam orbit position[a]	10.5 mm
Height of orbit bump	9 mm
Bumped beam position[a]	1.5 mm
Pulse width of the orbit bump[b]	3 μs
Pulse width of the septum magnet[b]	10 μs

[a]From the septum blade.
[b]Half-sine wave excitation.

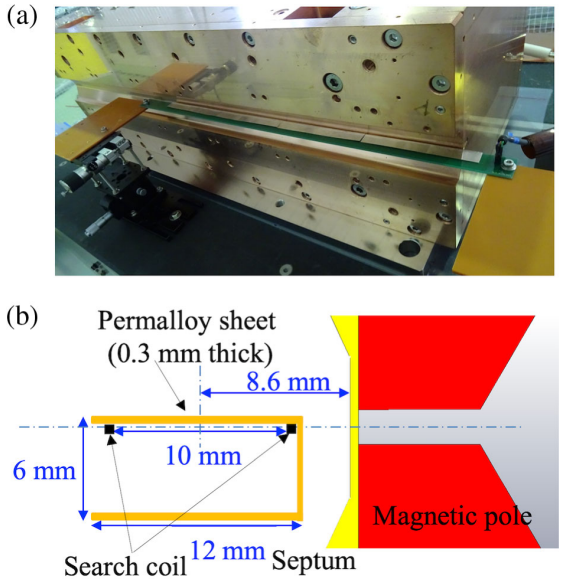


FIG. 18. Setup for a feasibility study on magnetic shielding with permalloy (Ni80Fe20) sheets. (a) The entire setup and (b) the cross-sectional arrangement of the search coil and the permalloy sheets.

a C-shape, and annealed to maintain the magnetic property. Four permalloy sheets were used to cover the 10 mm wide search coil placed adjacent to the septum blade, shielding a length of 400 mm. The average flux density in the search coil was evaluated by the value when it reached its maximum during the excitation of the septum magnet. The obtained flux densities without and with the permalloy sheets were 3.2×10^{-4} T and 9.2×10^{-6} T, respectively, corresponding to the attenuation factor of 35. The results of this feasibility study are promising. The thickness of the permalloy sheet can be increased up to 0.5 mm to obtain better shielding performance. The stray magnetic field target of 1×10^{-5} T m is considered achievable by implementing a magnetic shield with permalloy on the rf shield.

IV. VACUUM PERFORMANCE

For the vacuum performance assessment, the pulsed septum magnet was installed in the vacuum chamber with the rf shield attached to the magnet. The magnetic shields were omitted for this test as the primary objective was to evaluate outgassing from the laminated magnetic core. A bakeout was then conducted, during which the outer walls of the vacuum chamber were heated by sheathed heaters mounted on the exterior. K-type thermocouples were used to measure the temperatures of the rf shield and the magnet as well as the outer wall of the vacuum chamber. After the magnet reached a temperature of 150 °C, the temperature of the magnet was maintained for 72 h until the heating was stopped. The pressure history during the bakeout process is shown in Fig. 19, along with the temperature histories of the magnet, rf shield, and vacuum chamber. The pressure spikes on days 5 and 6 are due to degassing of the ion pump. After the NEG pump activation on day 7, a UHV pressure of 5×10^{-8} Pa was successfully achieved.

In addition to the vacuum pressure, the coupling impedance of the rf shield is an issue for maintaining stable electron beam circulation in the storage ring. An rf simulation was performed to assess the coupling impedance utilizing CST Studio Suite [23]. In the calculation, the lateral position of the stored beam was assumed to be 10 mm from the edge of the rf shield on the septum side, which corresponds to a distance of 10.5 mm from the septum blade assuming a thickness of the magnetic shielding sheet of 0.5 mm. The impedance spectrum was dominated by broadband components, without significant trapped modes that could cause narrowband resonances. Accordingly, the impact on the beam was evaluated using the effective impedance. The calculated effective impedance is illustrated in Fig. 20. The transverse effective impedance of the rf shield was smaller than 1 kΩ/m, and the longitudinal effective impedance was smaller than 1×10^{-4} Ω. In the preliminary impedance estimation for the latest vacuum chamber design of SPring-8-II, the total effective transverse impedances - $\langle \beta_{x,y} \rangle \, \mathrm{Im}\,(Z_{x,y})_{\mathrm{eff}}$ combined with the beta function, and the total effective longitudinal impedance $|Z_L/n|_{\mathrm{eff}}$ are estimated to be approximately 10 MΩ and 0.5 Ω, respectively. We concluded that the coupling impedance of the rf shield of the in-vacuum septum magnet of this work is within an acceptable range for the impedance budget

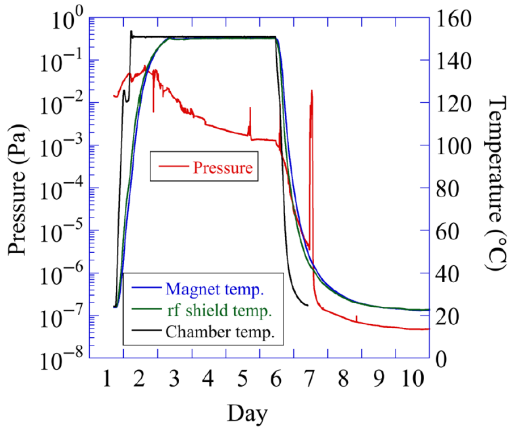


FIG. 19. Vacuum performance during and after a 72-h baking at 150 °C.

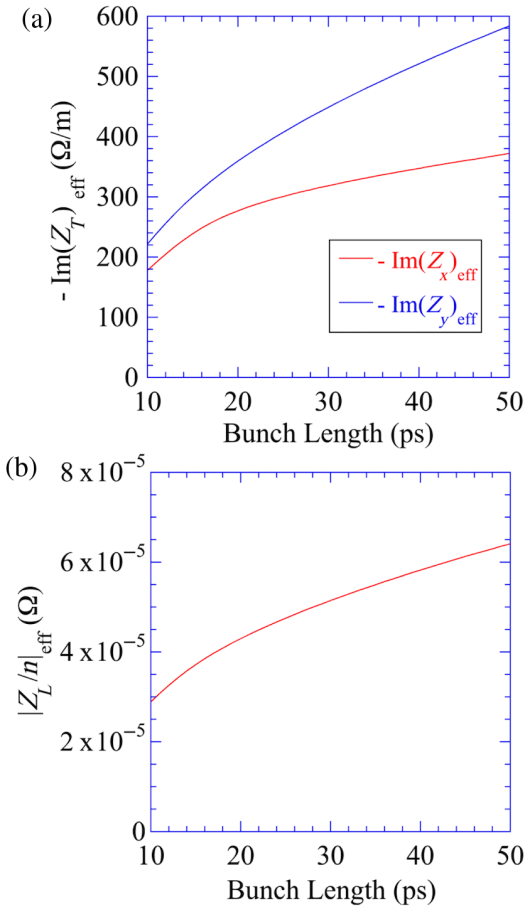


FIG. 20. Transverse (a) and longitudinal (b) effective impedance of the rf shield.

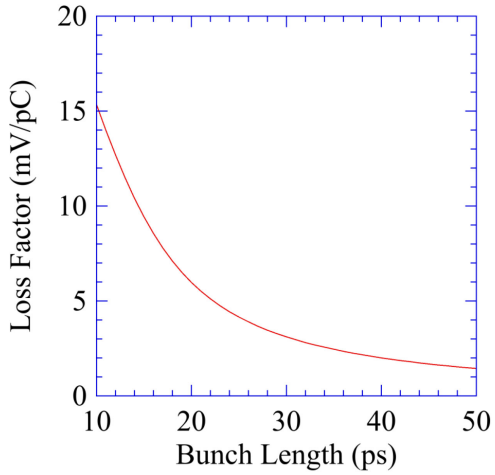


FIG. 21. Loss factor of the rf shield.

of SPring-8-II. The calculated loss factor of the rf shield is illustrated in Fig. 21. The heating of the rf shield by the stored beam was evaluated using a beam parameter assumed for the SPring-8-II storage ring: a total beam current of 200 mA in 406 uniform bunches of 14 ps length. The resulting heat was 5 W, which should be within the capacity of the indirect water cooling system depicted in Sec. II. B.

V. SUMMARY AND PROSPECT

Beam injection is one of the most crucial issues for next-generation light sources such as diffraction-limited storage rings (DLSRs). A novel transparent off-axis beam injection scheme is proposed to achieve efficient beam injection within the tight acceptance of the low-emittance storage ring by implementing small injection amplitude, while minimizing the perturbation to photon beams delivered to users. An in-vacuum thin eddy-current septum magnet is one of the key components in the scheme to achieve the small injection amplitude.

A prototype of the magnet has been developed in this work. The magnetic core of the pulsed septum magnet is designed with a narrow pole gap to maintain the beam deflection field uniformity in the gap as close to the septum blade as possible. The septum has a box-shaped configuration to minimize the stray magnetic field leakage from the magnetic core to the stored beam. The eddy-current septum magnet of this work features the thin design of the septum blade, as thin as 0.5 mm at the beam injection point. The rf shield for the stored beam is designed to suppress the coupling impedance to circulate the stored beam stably. The accommodating vacuum chamber with the vacuum pumps and the gauge is designed to provide indirect water cooling for the rf shield and the magnet.

The performance of the pulsed septum magnet was verified by gap field and stray field measurements. The gap field strength of 1.4 T was confirmed to be maintained even when the distance to the septum blade approached 1 mm, as designed. Stray magnetic field leakage to the stored beam measured outside the septum was in agreement with the simulations. Evaluations of the stray field strength acting on the bumped stored beam indicated the need for magnetic shielding on the rf shield. It was demonstrated that the target stray magnetic field of 1×10^{-5} T m or less can be achieved even at a position as close as 1.5 mm from the septum blade by implementing magnetic shielding with permalloy on the rf shield. Considering the thickness of the septum blade of 0.5 mm at the beam injection point, we conclude that an injection amplitude of only 3 mm is achievable with the thin eddy-current septum magnet developed in this work. A UHV pressure of 5×10^{-8} Pa was successfully achieved after 72 h of baking at 150 °C, thereby assuring vacuum performance essential to stable operation in the storage ring. The demonstrated performance of the prototype will hopefully pave the way for the use of in-vacuum thin eddy-current septum magnets for beam injection in next-generation light sources.

A new 3 GeV light source called NanoTerasu has been launched in Japan [24]. The in-vacuum thin eddy-current septum magnet developed in this work has been integrated into the beam injection section of the NanoTerasu storage ring to demonstrate its performance. The beam commissioning of NanoTerasu started in 2023. Beam injection and accumulation with the magnet have been successfully performed [25], contributing to the user operation of NanoTerasu since 2024. Detailed design of the in-vacuum thin eddy-current septum magnet for beam injection of SPring-8-II is ongoing.

ACKNOWLEDGMENTS

This work was supported by the JST Next Generation Accelerator Technology Development Program and the RIKEN SPring-8 Center (RSC).

DATA AVAILABILITY

The data that support the findings of this article are not publicly available. The data are available from the authors upon reasonable request.

[1] P. Raimondi, N. Carmignani, L. R. Carver, J. Chavanne, L. Farvacque, G. Le Bec, D. Martin, S. M. Liuzzo, T. Perron, and S. White, Commissioning of the hybrid multibend achromat lattice at the European Synchrotron Radiation Facility, Phys. Rev. Accel. Beams **24**, 110701 (2021).

[2] T. E. Fornek, Advanced photon source upgrade project final design report, Argonne National Laboratory (ANL),

Argonne, IL, Technical Report No. APSU-2.01-RPT-003, 2019, 10.2172/1543138.

[3] H. Tanaka *et al.*, Green upgrading of SPring-8 to produce stable, ultrabrilliant hard x-ray beams, J. Synchrotron Radiat. **31**, 1420 (2024).

[4] C. G. Schroer, I. Agapov, W. Brefeld, R. Brinkmann, Y-C. Chae, H-C. Chao, M. Eriksson, J. Keil, X. N. Gavaldà, R. Röhlsberger, O. H. Seeck, M. Sprung, M. Tischer, R. Wanzenberg, and E. Weckert, PETRA IV: The ultralow-emittance source project at DESY, J. Synchrotron Radiat. **25**, 1277 (2018).

[5] P. Raimondi and S. M. Liuzzo, Toward a diffraction limited light source, Phys. Rev. Accel. Beams **26**, 021601 (2023).

[6] T. Atkinson, M. Dirsat, O. Dressler, P. Kuske, and H. Rast, Development of a non-linear kicker system to facilitate a new injection scheme for the BESSY II storage ring, in *Proceedings of the 2nd International Particle Accelerator Conference, IPAC2011, San Sebastián, Spain, 2011* (JACoW, Geneva, Switzerland, 2011), pp. 3394–3396, https://proceedings.jacow.org/IPAC2011/papers/thpo024.pdf.

[7] P. Alexandre, R. B. E. Fekih, A. Letrésor, S. Thoraud, J. S. Castro, F. Bouvet, J. Breunlin, Å. Andersson, and P. F. Tavares, Transparent top-up injection into a fourth-generation storage ring, Nucl. Instrum. Methods Phys. Res., Sect. A **986**, 164739 (2021).

[8] L. Liu, M. B. Alves, F. C. Arroyo, G. O. Brunheira, G. R. Cruz, A. F. Giachero, A. C. S. Oliveira, F. S. de Oliveira, G. S. Ramirez, X. R. Resende, E. N. Rolim, F. H. de Sá, D. O. Tavares, and H. Westfahl, Jr., Status of SIRIUS operation with users, in *Proceedings of the 14th International Particle Accelerator Conference, IPAC-2023, Venice, Italy, 2023* (JACoW, Geneva, Switzerland, 2023), pp. 2586–2589, https://proceedings.jacow.org/ipac2023/pdf/WEOGA2.pdf.

[9] R. Ollier, P. Alexandre, R. Ben El Fekih, A. Gamelin, N. Hubert, M. Labat, L. S. Nadolski, and M.-A. Tordeux, Toward transparent injection with a multipole injection kicker in a storage ring, Phys. Rev. Accel. Beams **26**, 020101 (2023).

[10] V. Sajaev, M. Borland, J. Calvey, J. Dooling, L. Emery, K. Harkay, N. Kuklev, O. Mohsen, Y. Sun, N. Arnold, T. Berenc, A. Brill, H. Bui, J. Carwardine, W. Cheng, T. Fors, M. Kelly, R. Lindberg, G. Shen, M. Smith, F. Rafael, H. Shang, R. Soliday, U. Wienands, and B. Yang, Commissioning of the advanced photon source upgrade—The first swap-out injection-based synchrotron light source, in *Proceedings of the 16th International Particle Accelerator Conference, IPAC-2025, Taipei, Taiwan, 2025* (JACoW, Geneva, Switzerland, 2025), pp. 915–918.

[11] Z. Duan, J. Chen, Y. Y. Guo, D. H. Ji, Y. Jiao, C. Meng, Y. Peng, and G. Xu, Simulation of injection efficiency for the high energy photon source, in *Proceedings of the 10th International Particle Accelerator Conference, IPAC-2019, Melbourne, Australia, 2019* (JACoW, Geneva, Switzerland, 2019), pp. 1514–1517, https://proceedings.jacow.org/ipac2019/papers/tupgw048.pdf.

[12] P. Collier, Synchrotron phase space injection into LEP, in *Proceedings of the 1995 Particle Accelerator Conference and International Conference on High-Energy Accelerators, Dallas, TX, 1995* (IEEE, New York, NY, 1996), pp. 551–553, https://ieeexplore.ieee.org/abstract/document/504716.

[13] M. Aiba, B. Goddard, K. Oide, Y. Papaphilippou, Á. Saá Hernández, D. Shwartz, S. White, and F. Zimmermann, Top-up injection schemes for future circular lepton collider, Nucl. Instrum. Methods Phys. Res., Sect. A **880**, 98 (2018).

[14] S. Takano, K. Fukami, C. Kondo, M. Masaki, M. Oishi, M. Shoji, K. Tamura, T. Taniuchi, K. Yanagida, T. Watanabe, T. Hara, T. Inagaki, H. Tanaka, K. Hamato, J. Kataoka, K. Kusano, K. Ogata, Y. Saito, H. Akikawa, and K. Sato, Renovation of off-axis beam injection scheme for next-generation photon sources, in *Proceedings of the 10th International Particle Accelerator Conference, IPAC-2019, Melbourne, Australia, 2019* (JACoW, Geneva, Switzerland, 2019), pp. 2318–2321, https://proceedings.jacow.org/ipac2019/papers/wepmp009.pdf.

[15] H. Tanaka *et al.*, Stable top-up operation at SPring-8, J. Synchrotron Radiat. **13**, 378 (2006).

[16] T. Hara *et al.*, Low-emittance beam injection for a synchrotron radiation source using an x-ray free-electron laser linear accelerator, Phys. Rev. Accel. Beams **24**, 110702 (2021).

[17] T. Taniuchi, T. Watanabe, S. Takano, T. Aoki, K. Fukami, S. Matsubara, K. Yanagida, K. Hamato, J. Kataoka, K. Ogata, Y. Saito, and K. Kusano, dc septum magnet based on permanent magnet for next-generation light sources, Phys. Rev. Accel. Beams **23**, 012401 (2020).

[18] K. Fukami, T. Inagaki, T. Iwashita, H. Nakanishi, N. Nishimori, S. Takano, Y. Takemura, T. Taniuchi, T. Watanabe, H. Yamaguchi, and H. Tanaka, Iron lamination and interlaminar insulation for high-frequency pulsed magnets, Rev. Sci. Instrum. **93**, 023301 (2022).

[19] T. Inagaki, H. Tanaka, H. Akikawa, K. Sato, K. Fukami, C. Kondo, and S. Takano, Development of a solid-state pulse generator driving kicker magnets for a novel injection system of a low emittance storage ring, in *Proceedings of the 9th International Particle Accelerator Conference, IPAC-2018, Vancouver, BC, Canada* (JACoW, Geneva, Switzerland, 2018), pp. 1804–1807, https://proceedings.jacow.org/ipac2018/papers/weygbf4.pdf.

[20] P. Lebasque, P. Gros, J. P. Lavieville, J. Da Silva Castro, A. Mary, and D. Muller, Eddy current septum magnets for booster injection and extraction, and storage ring injection at synchrotron SOLEIL, in *Proceedings of 10th European Particle Accelerator Conference, Edinburgh, Scotland, 2006* (European Physical Society Accelerator Group, Mulhouse, France, 2006), pp. 3511–3513, https://proceedings.jacow.org/e06/PAPERS/THPLS101.pdf.

[21] L. Ouyang, M. Gu, B. Liu, and R. Cheng, Eddy current septum magnets for injection and extraction at SSRF, Chin. Phys. C **34**, 389 (2010).

[22] R. Ganter, SLS 2.0 storage ring upgrade overview, in *Proceedings of the 16th International Particle Accelerator Conference, IPAC-2025, Taipei, Taiwan* (JACoW, Geneva, Switzerland, 2025), pp. 79–82.

[23] Dassault Systemes, CST Studio Suite, https://www.3ds.com/products/simulia/cst-studio-suite.

[24] N. Nishimori, Recent development and future direction of ring-type synchrotron light sources in Japan, in *Proceedings of the 15th International Particle Accelerator Conference, IPAC-2024, Nashville, TN, 2024* (JACoW, Geneva, Switzerland, 2024), pp. 3939–3943, https://proceedings.jacow.org/ipac2024/pdf/FRYD2.pdf.

[25] S. Obara *et al.*, Commissioning of a compact multi-bend achromat lattice NanoTerasu: A new 3 GeV synchrotron radiation facility, Phys. Rev. Accel. Beams **28**, 020701 (2025).